ACS SENSORS

pubs.acs.org/acssensors

Article

One-Step Laser Nanostructuration of Reduced Graphene Oxide Films Embedding Metal Nanoparticles for Sensing Applications

Annalisa Scroccarello,[#] Ruslan Álvarez-Diduk,*[,#] Flavio Della Pelle, Cecilia de Carvalho Castro e Silva, Andrea Idili, Claudio Parolo, Dario Compagnone, and Arben Merkoçi*

Cite This: *ACS Sens.* 2023, 8, 598−609

Read Online

ACCESS | Metrics & More | Article Recommendations | Supporting Information

ABSTRACT: The combination of two-dimensional materials and metal nanoparticles (MNPs) allows the fabrication of novel nanocomposites with unique physical/chemical properties exploitable in high-performance smart devices and biosensing strategies. Current methods to obtain graphene-based films decorated with noble MNPs are cumbersome, poorly reproducible, and difficult to scale up. Herein, we propose a straightforward, versatile, surfactant-free, and single-step technique to produce reduced graphene oxide (rGO) conductive films integrating "naked" noble MNPs. This method relies on the instantaneous laser-induced co-reduction of graphene oxide and metal cations, resulting in highly exfoliated rGO nanosheets embedding gold, silver, and platinum NPs. The production procedure has been optimized, and the obtained nanomaterials are fully characterized; the hybrid nanosheets have been easily transferred onto lab-made screen-printed electrodes preserving their nanoarchitecture. The Au@rGO-, Ag@rGO-, and Pt@rGO-based electrodes have been challenged to detect caffeic acid, nitrite, and hydrogen peroxide in model solutions and real samples. The sensors yielded quantitative responses ($R^2 \geq 0.997$) with sub-micromolar limits of detections (LODs $\leq 0.6\ \mu$M) for all the analytes, allowing accurate quantification in samples (recoveries $\geq 90\%$; RSD $\leq 14.8\%$, $n = 3$). This single-step protocol which requires low cost and minimal equipment will allow the fabrication of free-standing, MNP-embedded rGO films integrable into a variety of scalable smart devices and biosensors.

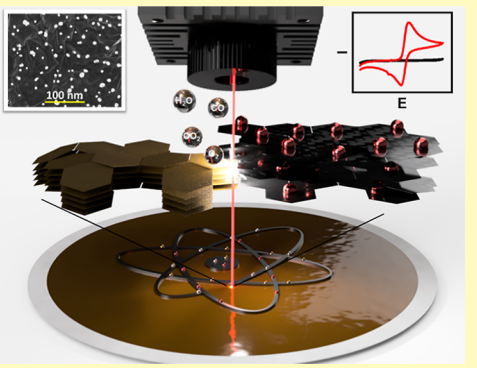

KEYWORDS: *laser reduced graphene oxide, IR-laser, nanodecoration, micropatterning, hybrid nanomaterials, surfactant-free, electrochemical sensor*

INTRODUCTION

Nanomaterials (NMs) have recently become major components of new electronic/optical smart devices and (bio)sensors because of the unique physical/chemical features that matter exhibits at the nanometer scale.[1,2] During the last two decades, metal nanoparticles (MNPs), thanks to their optical, mechanical, thermal, electrical, and physical properties, have been commonly used in several rapid diagnostic tests (e.g., lateral flow assays and fluorescent assays) and electronic appliances (e.g., smart-TVs).[1,3] Similarly, two-dimensional (2D) materials, in particular, graphene, having a unique surface-to-volume ratio and conductive properties, are also used in several (bio)sensing and smart devices. More recently, the research community has been focused on studying the properties of multicomponent and nanostructured materials with at least one dimension in the nanometer scale. In this respect, nanocomposites (NCs) originating from 2D materials, in particular, graphene/graphene derivatives (i.e., graphene oxide) and MNPs, proved to possess useful features; these have been exploited to develop sensing substrates for optical,[4,5] electrochemical,[6−9] and gas[10−12] sensors that have been successfully used for different applications. Despite their peculiar and promising properties, the implementation of these hybrid NMs outside the research laboratories is still very limited.

Overall, the methods to synthesize NMs can be categorized into bottom-up and top-down approaches. The former consists of assembling atoms into ordered nanostructures requiring accurate control of all reaction conditions (e.g., substrate concentration, pH, and temperature), while the latter consists of breaking down bulk materials into nanosized structures. Bottom-up approaches are generally used for the synthesis of MNPs; on the other hand, top-down approaches are generally more convenient for the fabrication of 2D materials (e.g., graphene) since they provide higher yield and an easier procedure.[13−16] Studies aiming at fabricating NCs made of 2D materials and MNPs rely on the separate synthesis of NMs and their combination via physical adsorption or chemical

Received: August 17, 2022
Accepted: November 8, 2022
Published: February 3, 2023

interactions.[17−19] It is also possible to perform the in situ synthesis of MNPs onto the hosting NM (e.g., reduction of metal ions mediated by an external reducing agent or by the substrate itself, galvanic displacement, etc.).[19−21] Although these two strategies generally guarantee effective nanodecorations, they also imply three main limitations: (i) the use of external reducing compounds and capping agents that interact intimately with the MNP surface to stabilize them, often masking their properties as their electrical/electrochemical properties; (ii) limited control over the decoration pattern and MNP distribution; and (iii) needing cumbersome and multistep procedures, making the whole process costly and time-consuming and, therefore, not suitable for the majority of commercial applications.

In this framework, in the last decade, laser-based processing technologies demonstrated tremendous potential for the patterning, structuring, and property tuning of NMs (e.g., doping, reduction, etc.).[22−29] In this context, different laser sources have been employed, among which the IR-laser is the most appealing due to the emitted energy, the low cost, and ease of management. These aspects have bumped highly automated IR-laser plotters into the market.

The IR-laser has been strongly employed to process carbon-based nanostructures; IR-laser-based technologies can produce graphene by triggering photothermal events to carbon-containing substrates (i.e., hydrocarbon cyclic skeleton or aromatic heterocycles), inducing graphitization processes that consist of weak bond breaking and induction of sp^2 nanostructured domains.[24,26−28] Although several studies report the use of the IR-laser to synthesize graphene or tune its properties, very few report the use of the IR-laser to simultaneously produce and nanodecorate the "graphene-based/like" structure with MNPs.[23,30]

Recently, Ye et al.[30] carried out the first laser-induced graphene production and simultaneous decoration with metal oxides, using a polyimide film embedded with metal complexes as precursors. You et al.[23] fabricated interdigitated array electrodes exploiting the laser scribing patterning and ability to trigger graphitization from the polyimide film and to simultaneously reduce noble MNPs. In both cases, the laser treatment and MNP decoration occur in situ and are localized to the substrate's shallow. Then, there is a clear need to investigate new methods to obtain, in a single step, a graphene nanostructure decorated with NMs easily transferable to any substrate, allowing us to develop different types of (opto)-electronic and electrochemical devices, also on a large scale.

In this paper, we propose a strategy to produce, in a single step, a freestanding film of reduced graphene oxide (rGO) decorated with three different metal nanoparticles (AuNPs, AgNPs, and PtNPs). The IR-laser was used to simultaneously and accurately produce a highly exfoliated rGO substrate and in situ decorate it with naked MNPs. After presenting the careful optimization of the method and the full characterization of the nanocomposites, we also demonstrate how they can be successfully integrated into flexible substrates to fabricate functional electrodes. Finally, the resulting electrochemical sensors were used to detect caffeic acid, nitrite, and hydrogen peroxide in samples. Thanks to its low cost and ease of use, we believe that our method can represent the solution to produce high amounts of high-quality rGO films decorated with MNPs.

MATERIALS AND METHODS

Reagents and Stock Solution. A detailed description of all the reagents and stock solutions used is reported in the Supporting Information (Section S1.1).

Apparatus. The laser plotter employed was a Rayjet50 laser machine from Trotec (Wels, Austria) equipped with a CO_2 laser (10.6 μm, 30 W, laser spot of 0.04 mm). The nanodecorated film patterns were designed with Corel Draw software. Vacuum filtration was performed through a 1 L vacuum-filtering flask, equipped with a 300 mL glass filter holder and 47 mm SS screen (1/*Pk*) from Millipore and a vacuum pump from KNF LAB LABOPORT. Press transfer and electrode screen printing were carried out using a laboratory hydraulic press and a screen printer machine, respectively.

Laser-Assisted MNPs@rGO Film Formation. Working solutions of 30 mM gold/Au(III), 15 mM silver/Ag(I), and 30 mM platinum/Pt(II) salt were prepared in Milli-Q water and promptly used. To produce the M^{n+}@GO film, 0.4 mL of a 10 mg mL^{-1} GO stock solution was diluted with 5 mL of the respective metal salt solution; the dispersion was then stirred for 5 min and filtered onto a polyvinylidene fluoride (PVDF) membrane (0.1 μm pore size and 47 mm diameter). The filtered material film was let to dry at room temperature for 20 min. After drying, the film was aligned according to the patterned design and treated with the CO_2 laser under a 7.4 cm focusing lens, using the engraving mode (laser power 2.10 W and speed 1.50 m s^{-1}). A pattern of 17 key-lock-like working electrodes (WE, Ø = 3 mm), obtained using Corel Draw software, was used for "laser scribing". A GO film formed with the same procedure without the metal source was used as the control; the latter was produced by filtering 0.4 mL of 10 mg mL^{-1} GO stock solution diluted in 5 mL of Milli-Q water.

Sensor Fabrication. The sensors were assembled to form complete three-electrode electrochemical cells with the laser-treated films used as working electrodes (WE).

The film (with the key-lock pattern) was cut in small rectangles through the CO_2 laser using the engraving mode (power 7.60 W and speed 0.75 m s^{-1}). A polyethylene terephthalate (PET) sheet was used as the sensor base, and the PET was cleaned with a 95% ethanolic solution before use. The electrical contacts and the reference electrode were screen-printed onto the PET sheet using conductive silver ink, whereas the counter electrode was made from carbon sensor paste. The WE pattern was aligned above the electrode surface according to the WE position. The nanostructured film was transferred onto the PET substrate by applying a pressure of 3.0 ± 0.1 t for 3 min using a hydraulic press. Finally, the PVDF filter was removed, and the contacts were insulated using a dielectric insulating paint. The sensor component size is reported in Figure S9.

Morphological and Chemical Characterization. For the morphological and elemental characterization of the generated nanostructured films, a Magellan 400L XHR SEM (FEI, Hillsboro, OR) instrument and a Quanta 650 FEG ESEM (FEI, Hillsboro, OR) instrument were used for scanning electron microscopy (SEM) and energy-dispersive X-ray spectroscopy (EDX) analysis. The MNP size distribution (calculated on an average number of 200 MNPs) was evaluated with "ImageJ, v.1.49.p". X-ray photoelectron spectroscopy (XPS) measurements were performed using a SPECS PHOIBOS 150 hemispherical analyzer (SPECS GmbH, Berlin, Germany), with a base pressure of 5×10^{-10} mbar, using a monochromatic Al K-alpha radiation (1486.74 eV) as the excitation source. The XPS spectral deconvolution and the identification of the peaks were run—following the technique described by Sen et al.[31]—through the Gaussian−Lorentzian fitting method, after smoothing and subtraction of the Shirley-shaped background. A confocal Raman spectrometer alpha300r (WITec, Ulm, German) equipped with a 488 nm laser, using a 1.5 mW laser power, a grating 600 g/nm, and objective 50×, was employed, using an exposure time of 10 s and three accumulations for each spectrum.

Electrochemical Measurements. Electrochemical experiments were carried out using an AutoLab PGStat302 equipped with NOVA 2.1.3 (Metrohm AutoLab) software. The chemistry of the laser-formed nanostructured films was assessed by CV in 0.5 M H_2SO_4 for Au@rGO

https://doi.org/10.1021/acssensors.2c01782
ACS Sens. 2023, 8, 598−609

and Pt@rGO, while in 0.1 M KCl for the Ag@rGO; in all the cases, a scan rate of 100 mV s^{-1} was adopted. The electrochemical characterization of the nanostructured sensors was carried out using cyclic voltammetry and electrochemical impedance spectroscopy using $Fe(CN)_6^{2-/3-}$ and $Ru(NH_3)_6^{3+/2+}$ at 3 mM in KCl 0.1 M as redox probes. EIS was conducted at open circuit potential, with a ±10 mV amplitude sinusoidal wave, scanning the 10^{-2} to 10^5 Hz frequency range. All the explorative CVs for both redox probes and analytes (caffeic acid, nitrite, and H_2O_2) were performed at 25 mV s^{-1}. Differential pulse voltammetry (DPV) in 0.1 M phosphate buffer with 0.1 M KCl (PB) was employed to quantify caffeic acid (pH 7.0) and nitrite (pH 4.0), using a pulse width of 50 ms, a modulation amplitude of 50 mV, with a resulting scan rate of 25 mV s^{-1}. Chronoamperometry was employed to quantify H_2O_2 in PB (pH 7.0), the measurement encompassed an electrode preconditioning at +0.8 V (60 s) followed by amperometry at 0.0 V, and the signal was recorded at 60 s. All the electrochemical measurements were performed versus pseudo-Ag/AgCl reference electrode in triplicate, placing a 100 μL drop of the solution to analyze on the top of the integrated electrochemical cell.

MNPs@rGO-Based Sensor for Caffeic Acid, NO_2^-, and H_2O_2 Evaluation. Quantification of caffeic acid (CA) in a coffee sample and of nitrite in fishing lake water (Lago Paradiso, Mosciano Sant'Angelo, Teramo, Italy) was accomplished by DPV (same parameters as the Electrochemical Measurements section) using the Au@rGO- and Ag@rGO-based sensors, respectively. The samples' pretreatment procedures are described in detail in Section S1.2; DPV measurements were performed by diluting the sample extract in PB (at the pH indicated in the Electrochemical Measurements section).

H_2O_2 determination was used to assess in-door disinfection fogging treatment residues. The treatment was performed according to EU guidelines,[32] and the decay of the H_2O_2 residue over time was evaluated onto a surface of 2 cm^2 using a dedicated adhesive surface delimiter (detailed description in Section S1.2). After fogging, 200 μL of PB (pH 7.0) was placed in the surface delimiter for 1 min and directly used for the H_2O_2 residue quantification transferring 100 μL onto the Pt@rGO. The same amperometric procedure described in the Electrochemical Measurements section was used for the measurement. The H_2O_2 surface residues were evaluated immediately after the fogging treatment and after 15 and 30 min.

RESULTS AND DISCUSSION

This work aims to propose a straightforward strategy to produce transferable nanostructured films to design effective lab-made sensors for different applications. To achieve this goal, reduced graphene oxide (rGO) was chosen for the structural features and intrinsic conductivity, while the decoration with different MNPs was exploited to improve the performance and give additional catalytic activities; controlled laser scribing was used as the film production technique.

rGO Film Fabrication and Characterization. The laser-induced nanostructured film formation was carried out starting from a graphene oxide (GO) film incorporating noble metal cations (M^{n+}@GO), and a sketch of the MNPs@rGO sensor fabrication is shown in Figure 1. A detailed description of the fabrication procedure is reported in the Laser-Assisted MNPs@rGO Film Formation section. Furthermore, an overview video of the fabrication process can be seen in Video S1.

The laser treatment conditions were carefully optimized to obtain a homogeneous and reproducible rGO film (see Section S2). Figure 2 reports the SEM images of the GO film before and after the laser treatment. The GO film shows a smooth and uniform structure with no evidence of lamellar nanostructures; at this stage, the film is nonconductive.

After the laser treatment and press-transfer of the film onto the PET substrate (see the Sensors Fabrication section), the structure of the film appears wrinkled and is characterized by the presence of highly exfoliated flakes with a nanometric section.

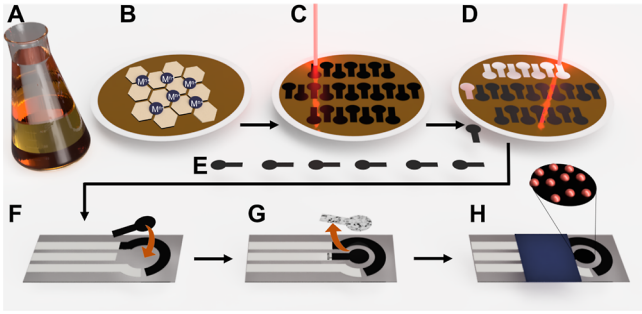

Figure 1. Sketch of the MNPs@rGO film formation and sensor fabrication. (A) GO mixing with metal precursor (M^{n+}); (B) M^{n+}@GO film formed after vacuum co-filtration of M^{n+} and GO; (C) laser-mediated reduction of the M^{n+}@GO film according to the working electrode design; (D) formed MNPs@rGO-based working electrode laser cutting; (F) working electrode alignment and transfer onto the PET screen-printed electrode; (G) working electrode remaining's remotion; and (H) complete MNPs@rGO sensor.

Figure 2A shows the SEM image of the rGO film after being transferred to the PET substrate. Clearly, even after the transfer, the rGO film preserves its highly exfoliated structure.

In order to evaluate the effect of the laser treatment on GO, the EDX elemental analysis, Raman spectroscopy, and X-ray photoelectron spectroscopy were carried out. The EDX elemental characterization of the film confirms a reduction of GO to rGO after laser treatment since the C amount in the elemental composition EDX moved from 83.7% for the GO film (Figure S2) to 100% for the rGO (Figure 2A). The Raman spectra (Figure 2B) gave the classical Raman features for GO and rGO, consisting of a D band at ∼1350 cm^{-1}, resulting from the sp^3 carbons from defects, the G band at ∼1580 cm^{-1}, attributed to the sp^2 carbons (refers to the stretching of the C−C bonds), and the 2D band (∼2700 cm^{-1}) for the rGO, that is directly related to the structural organization in the two-dimensional plane of graphene derivatives.[33] It is evident how the $I(D)/I(G)$ ratio decreases after laser treatment, from 0.92 ± 0.05 (GO film) to 0.64 ± 0.06 (rGO); this confirms the increase in the $-sp^2$ carbon domain compared to the $-sp^3$. Besides, the fitting of the rGO 2D band and the full width at half-maximum value (∼76 cm^{-1}) are compatible with randomly stacked single-layer graphene (around five layers ∼75 cm^{-1});[36] thus, it is possible to affirm that the laser treatment (due to the high heating effect) promotes the expansion of the rGO sheets in the film, increasing their exfoliation.[22,27,37] This is evident from the SEM micrographs for the GO (Figure S2) and rGO (Figure 2A) films. XPS analysis of the GO film before (Figure 2C) and after (Figure 2D) the treatment confirms the efficiency of the chemical reduction of the GO.[38] Before GO treatment, the C1s high-resolution spectrum highlights C−C carbon at a binding energy (BE) of 284.2 eV and oxygen-containing functional groups at 286.3 and 288.1 eV, corresponding to hydroxyl/epoxy carbon groups (C−O) and carbonyl groups (C═O), respectively. After the laser treatment, the C1s spectrum demonstrates the GO reduction, with the carbon sharp peak observed at 284.6 eV related to sp^2-hybridized carbon (C═C), and a substantial decrease of 61% for the C−O (286.7 eV) and of 10% for C═O (288.4 eV).[39,40] This proves that highly exfoliated rGO can be produced starting from GO by laser treatment.[22,27]

MNPs@rGO Film Fabrication and Characterization. The MNPs@rGO fabrication was carefully optimized for each

https://doi.org/10.1021/acssensors.2c01782
ACS Sens. 2023, 8, 598−609

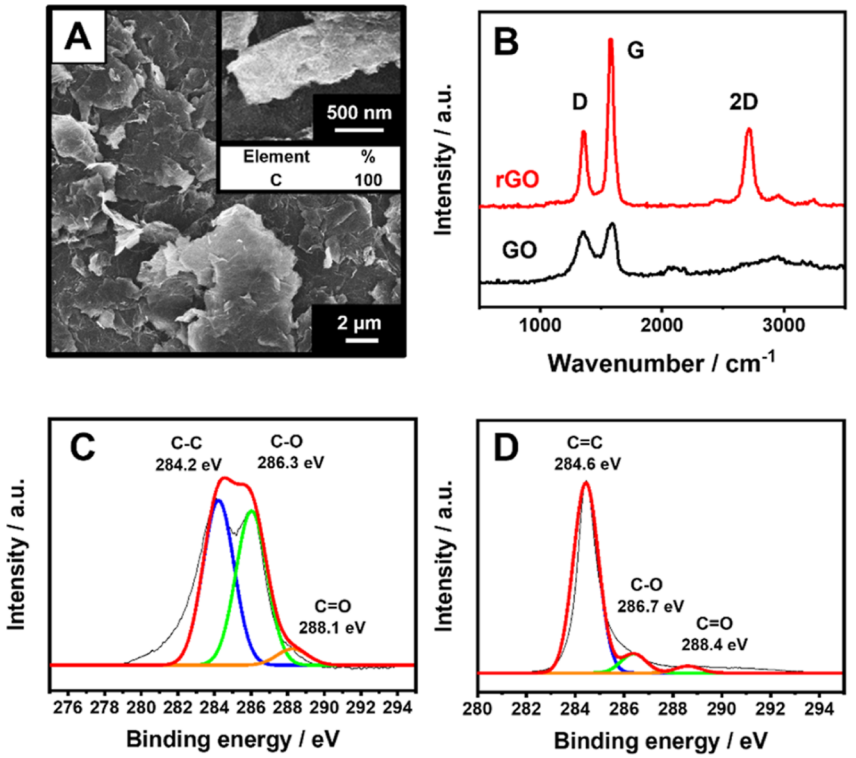

Figure 2. (A) SEM micrograph of the GO film after laser treatment. The inset reports a magnification of the rGO film and the % elemental composition. (B) Raman spectra of the GO (black line) and rGO (red line) film. (C) C 1s XPS spectrum of the GO film. (D) C 1s XPS spectrum of the rGO film obtained via laser treatment. All the analyses were performed after the film integration into the sensor.

nanocomposite. GO and the metal ion (i.e., Au(III), Ag(I), and Pt(II)) were co-filtered; then, the film was "one-shot" reduced via CO_2 laser-engraving and transferred onto the PET sensor support. To obtain well-distributed MNPs on the rGO film, the amount of GO, metal salt, and the number of laser cycles were thoroughly optimized for each nanocomposite; a detailed description of the optimization is reported in Section S3 and Table S1.

Figure 3 shows SEM magnifications of the Au@rGO (Figure 3A), Ag@rGO (Figure 3B), and Pt@rGO (Figure 3C) obtained by employing the optimized conditions. The AuNPs and AgNPs are round-shaped with a mean diameter of 9 ± 1 and 32 ± 2 nm, respectively, whereas the Pt@rGO film shows cubic PtNPs with a mean lateral size of 15 ± 1 nm (Figure 3D–F). The EDX analysis confirmed the AuNPs', AgNPs', and PtNPs' presence; Figure S3 reports the elemental color mapping of the MNPs@rGO films, highlighting the AuNPs', AgNPs', and PtNPs' uniform distribution on the rGO film. The homogeneous MNP distribution onto the rGO film can be attributed to the spatial distribution of the metal cations on the GO surface and the uniformity of the laser treatment. In this context, Zhao and Zhu[41] demonstrated graphene's ability to establish cationic-π interactions along with the whole aromatic ring structure. The cations are further retained by the GO coordination chemistry driven by the presence of epoxy groups on the GO surface and the oxygenated nucleophilic groups along the flake borders.[41−43]

The GO reduction to rGO was also confirmed in the presence of the metal salts for all the nanocomposites by XPS analysis (Figure S4A–C). The valence state of the Au, Ag, and Pt on the graphene bed was studied before and after the laser treatment; in Figure S4, the spectra of the M^{n+}@GO nanocomposites are reported, while Figure 3G–I shows the spectra after the treatment (MNPs@rGO).

For the Au(III)@GO before the laser treatment, two solved components at BEs of 85.6 and 89.2 eV corresponding to the Au $4f_{7/2}$ (Au^{3+}) and Au $4f_{5/2}$ (Au^{1+}) electron doublet, respectively, are observed (Figure S4D).[40,44,45] Despite the fact that the cation used is the Au(III), the presence of Au(I) can be attributed to the GO coordination ability through cation-π and electrostatic interactions.[34,41,46−48] A slight presence of zerovalent Au(0) was detected by XPS at 83.7 eV, which can be attributed to the intrinsic chemistry of the GO rich in vacant electrons, electron doublets, and electronegative functional groups potentially able to reduce the Au^{3+} to Au^0, promoting the production of Au nanoseeds.[42,47,48] After the laser (Figure 3G), the AuNP formation is suggested by the BE shift toward lower values.[44] The two sharp and asymmetric peaks recorded at 84.0 and 87.7 eV, with a spin−orbit splitting value of 3.7 eV, are characteristic of the Au(0).[23,49,50]

Looking at Ag@rGO formation (Figure 3H), the Ag oxidation state passes from +1 (Ag(I)@GO) to 0 (Ag@rGO), and this is observable by the BE shifting to larger values: from 364.8 to 368.4 eV for $Ag3d_{5/2}$ and from 370.9 to 374.3 eV for $Ag3d_{3/2}$.[40,49,51,52] The peak asymmetry and a separation value of 5.9 eV (Figure 3H) confirm the Ag presence in the metallic form.[49,53,54] In the Ag@rGO, oxides of Ag are not observed, indicating that the laser exclusively produced AgNPs.[52]

The Pt valence states on the GO (before laser) and rGO (after laser) films were studied through the Pt 4f electron spectra. Before the laser treatment, the Pt 4f spectra have three peaks at 70.7, 73.2, and 75.8 eV (Figure S4F) assigned to Pt(0), Pt(II), and Pt(IV), respectively.[55,56] A very small fraction of Pt(0) is observed in agreement with the chemisorption capability of GO.[34] After the laser treatment (Figure 3I), the synthesis of PtNPs was confirmed by a positive shift of the Pt 4f peaks to BEs of 71.4 eV (Pt $4f_{7/2}$) and 74.5 eV (Pt $4f_{5/2}$), with a spin−orbit

https://doi.org/10.1021/acssensors.2c01782
ACS Sens. 2023, 8, 598−609

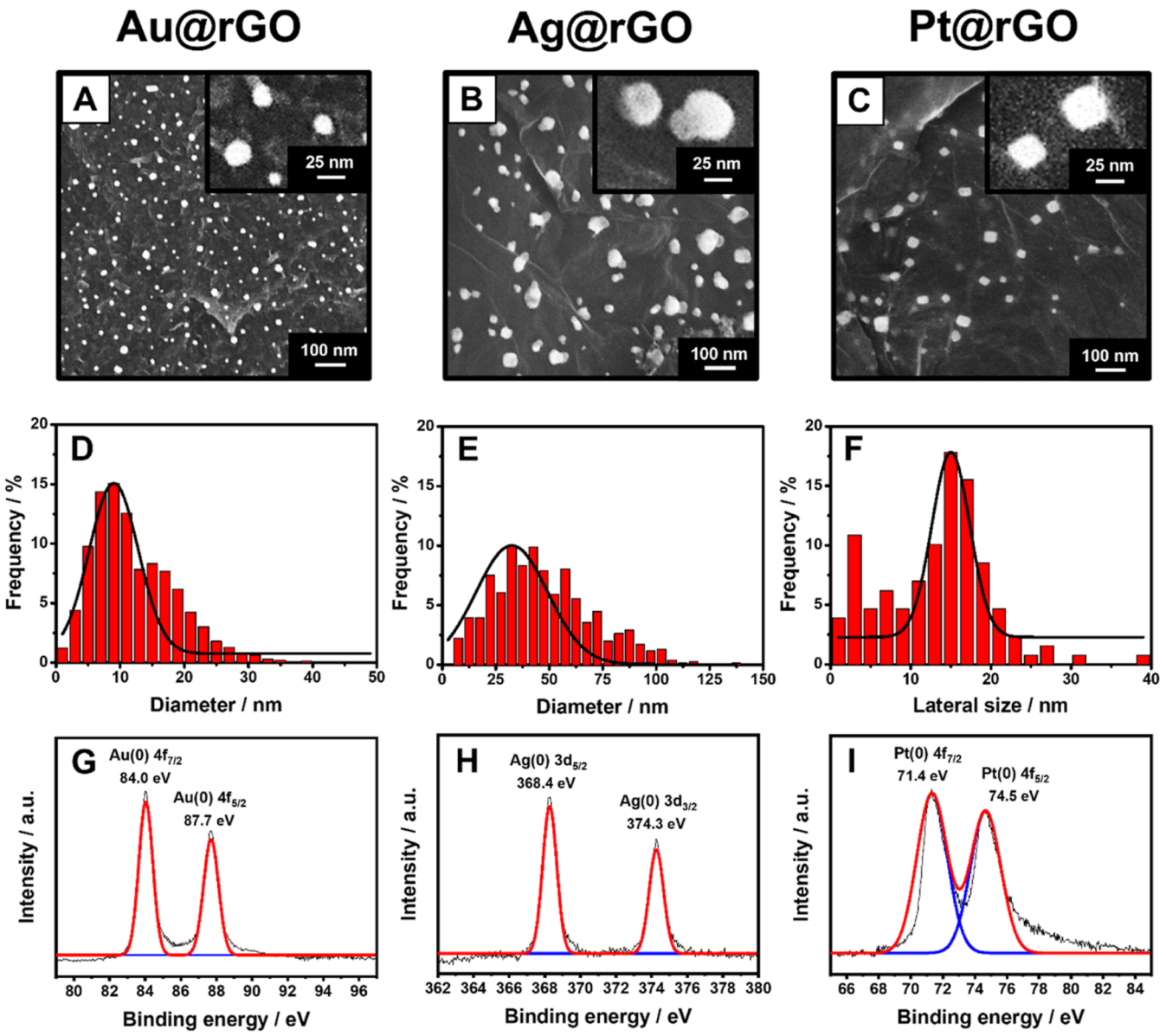

Figure 3. SEM micrographs of the (A) Au@rGO, (B) Ag@rGO, and (C) Pt@rGO films. The insets report a magnification of the formed MNPs. Size distribution of (D) AuNP, (E) AgNP, and (F) PtNP population onto the respective film. XPS spectra of the MNPs@rGO films formed with the laser treatment. (G) XPS spectrum of the Au 4f of the Au@rGO film. (H) XPS spectrum of the Ag 3d of the Ag@rGO film. (I) XPS spectrum of Pt 4f XPS spectra of the Pt@rGO films. All the analyses were performed after the film integration into the sensor.

splitting value of 3.1 eV, which is close to the metallic value (Δ = 3.4 eV).[57,58] Despite the fact that the Pt salt can form coordination complexes, the full reduction of the Pt precursor was confirmed by the Pt $4f_{7/2}$ binding energy (71.4 eV) quite similar to the bulk platinum one (71.2 eV).[23,59]

MNPs@rGO Formation Mechanism Proposal. A hypothesis about the laser-mediated MNPs@rGO formation is illustrated in Figure 4 and described below.

The CO_2-laser beam, in the near IR region (λ = 10.6 μm), induces a photothermal process able to remove the oxygen-containing groups and lattice defects typical of the GO, driving the whole restoration of the sp^2 domain[24,60−62] proper of graphene structures[25−28,63] and leading to the formation of rGO. We speculate that the MNPs@rGO formation is the result of an instantaneous cascade of events summarized as follows. The laser interacts with the GO film and drastically increases the local temperature, inducing the atom thermal excitation with consequent oxygen group elimination (in the form of O_2, CO, CO_2, and H_2O).[60] The fast and violent expelling of oxygen-containing groups leads to the GO flake cracking and de-stacking; for this reason, the laser-treated zone physically expands, becoming exfoliated.[64,65] Simultaneously, the energy

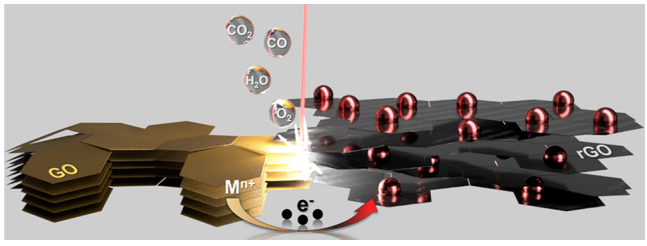

Figure 4. Sketch of the proposed MNPs@rGO mechanism of nanostructured film formation.

https://doi.org/10.1021/acssensors.2c01782
ACS Sens. 2023, 8, 598−609

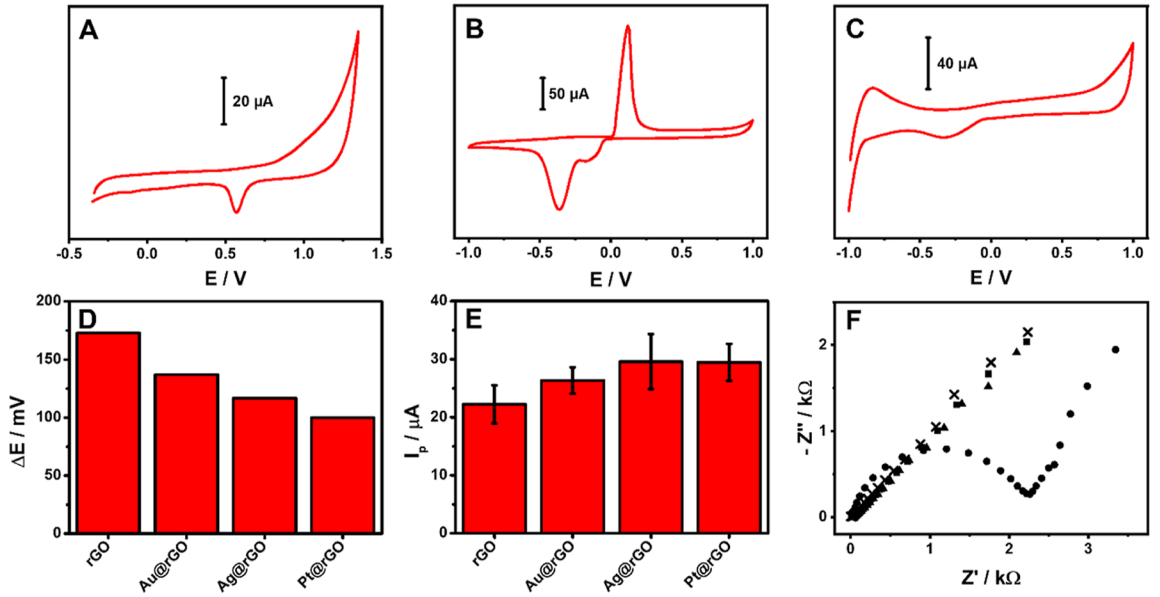

Figure 5. (A) Cyclic voltammogram of the Au@rGO sensor in 0.5 M H_2SO_4. (B) Cyclic voltammogram of the Ag@rGO sensor in 0.1 M KCl. (C) Cyclic voltammogram of the Pt@rGO sensor in 0.5 M H_2SO_4. All the sensors' CVs were performed at 100 mV s^{-1}. (D) Peak-to-peak separation potential (ΔE) and (E) anodic peak intensity extrapolated from CVs performed in 3 mM $Fe(CN)_6^{2-/3-}$ in KCl 0.1 M at 25 mV s^{-1} using the proposed rGO and MNPs@rGO-based sensors. (F) Nyquist plots obtained from EIS analysis performed in 3 mM $Fe(CN)_6^{4-/3-}$ in 0.1 M KCl with the sensors integrating the rGO (●), Au@rGO (▲), Ag@rGO (×), and Pt@rGO (■) films.

provided by the laser is sufficient to trigger the reduction of the metal source to the metal zero-valent state, where the electron transfer process is favored by the intimate cation-π interaction between the GO and the metal cations.[41−43] We suppose that the photothermal energy produces electron excitation in the graphene, which, being rich in p-orbitals, is prone to host and/or exchange electrons playing the role of electron donor to the metal cations.[42,66] Then, the metal ions are first reduced to metallic nuclei, which subsequently combine into MNPs up to reaching critical dimensions that result to be energetically favored.[41−43] The outcome is naked MNPs, uniformly distributed and strongly anchored on the rGO substrate.[62]

MNPs@rGO Sensor Electrochemical Characterization. The integrated MNPs@rGO sensor fabrication is described in detail in the Laser-Assisted MNPs@rGO Film Formation section, and the main steps are summarized in Figure 1. The electrochemical profile of the MNPs@rGO-based sensors was initially evaluated to highlight the crude chemistry of the nanocomposite; bare rGO is reported in Figure S5. As illustrated in Figure 5A−C, the presence of Au, Ag, and Pt nanostructures is confirmed by the characteristic oxidation and/or reduction peaks observed;[46,67] the latter is not observed for the bare rGO.

The obtained MNPs are electrochemically stable and strongly anchored to the rGO; in fact, after 50 consecutive CVs performed in 0.5 M H_2SO_4, for Au@rGO and Pt@rGO, and 0.1 M KCl for Ag@rGO, the characteristic metal peaks showed a signal recovery of 99% (Au@rGO), 96% (Ag@rGO), and 88% (Pt@rGO) compared to the starting intensity (Figure S6). The MNPs@rGO stability was further assessed by simulating a discontinuous use of the sensors; consecutive independent CV cycles (five scans each) have been run ten times; among measuring cycles, the electrode was dried under environmental conditions. Signal recoveries of 94% (Au@rGO), 91% (Ag@rGO), and 83% (Pt@rGO) were obtained. The sensors' long-term stability was eventually studied over 3 months (measuring each week), keeping the sensors at room temperature and protected from light (Figure S6). The electrochemical response retention for all the sensors over time (3 months) was studied following the anodic peak intensity and the peak-to-peak separation using $Fe(CN)_6^{2-/3-}$ as the probe. After 3 months, a slight ΔE broadening was observed for all the sensors (100 ± 8, 120 ± 8, and 147 ± 16 mV for Pt@rGO, Ag@rGO, and Au@rGO, respectively), while the peak intensity was quite stable compared to the initial (anodic peak height retention ≥ 93%).

The morphological nanostructures' stability, both after consecutive measurement and after storage, was assessed by SEM observations as well, and no significant variations were observed, further confirming that the MNPs were strongly anchored and stabilized by the rGO substrate (Figure S6).

The electron transfer ability of the MNPs@rGO sensors was investigated as compared to that of bare rGO employing inner- and outer-sphere redox probes, that is, the ferro/ferricyanide ($Fe(CN)_6^{2-/3-}$) and the ruthenium couple ($Ru(NH_3)_6^{3+/2+}$). The cyclic voltammograms obtained for both probes are reported in Figure S7, and the extrapolated parameters are listed in Table S2. For a better comparison of the sensors' behavior, Figure 5D,E shows the graph of the peak-to-peak separation (ΔE) and the anodic peak intensity obtained for the ferro/ferricyanide.

The $Fe(CN)_6^{2-/3-}$ intimately interacts with the sensor surface, and the electron transfer occurs directly via the redox probe adsorption on the used material;[68] a quasi-reversible behavior was obtained for all the sensors, and a significant ΔE decrease was observed from rGO (ΔE = 173 mV) to the MNPs@rGO. The best improvement was obtained with the Pt@rGO with a ΔE of 100 mV, immediately followed by Ag@rGO (ΔE = 117 mV) and Au@rGO (ΔE = 137 mV). The peak-to-peak separation, an index of the electron transfer ability, is consistent with the metal features expected (Pt > Ag > Au).[34,35] As depicted in Figure 5E, the anodic peak intensity follows the opposite behavior of the ΔE, and for all the sensors, the anodic/cathodic peak intensity ratio is close to 1.

https://doi.org/10.1021/acssensors.2c01782
ACS Sens. 2023, 8, 598−609

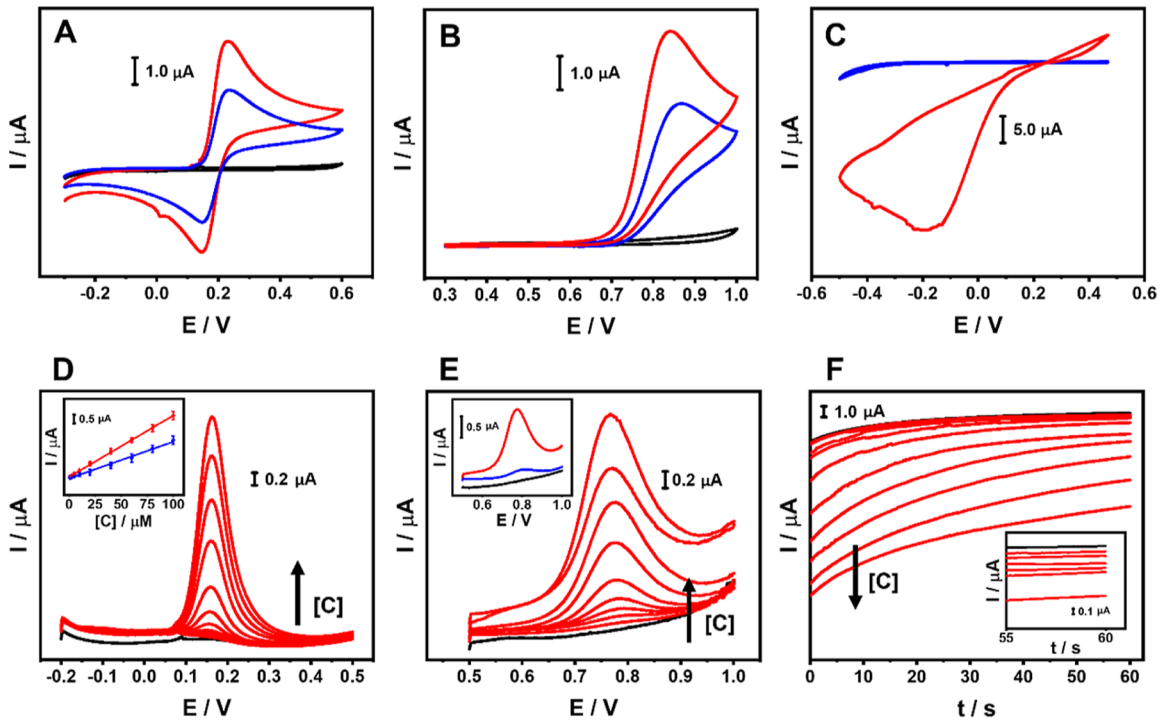

Figure 6. (A) Cyclic voltammograms of 250 μM CA in PB + 0.1 M KCl (pH 7.0) performed with the rGO- (blue line) and Au@rGO (red line)-based sensors. (B) Cyclic voltammograms of 250 μM NO_2^- in PB + 0.1 M KCl (pH 4.0) performed with the rGO- (blue line) and Ag@rGO (red line)-based sensors. (C) Cyclic voltammograms of 250 μM H_2O_2 in PB + 0.1 M KCl (pH 7.0) performed with the rGO- (blue line) and Pt@rGO (red line)-based sensors. All the CVs were performed at 25 mV s^{-1}; the black curve represents the blank measure performed with the used MNPs@rGO sensor. (D) DP voltammograms of CA from 0.5 to 100 μM at the Au@rGO sensor (in PB + 0.1 M KCl; pH 7.0). The black curve corresponds to the blank. The inset reports the calibration curve comparison between Au@rGO- (red line) and rGO (blue line)-based sensors. (E) DP voltammograms of NO_2^- from 1 to 100 μM at the Ag@rGO sensor (in PB + 0.1 M KCl; pH 4.0). The black curve corresponds to the blank. The inset reports the DP voltammograms of 60 μM NO_2^- at the Ag@rGO- (red curve) and rGO (blue curve)-based sensor. (F) Chronoamperograms obtained for the H_2O_2 from 5 to 2000 μM (in PB + 0.1 M KCl; pH 7.0). The black curve corresponds to the blank. The inset reports the magnification of the first six points tested (from 5 to 250 μM).

To further explore the sensors' electrochemical features, the electroactive surface area (ECSA) of the MNPs@rGO sensors was calculated according to Randles−Sevick's theory for quasi-reversible systems,[69,70] and ECSAs of 8.20 ± 0.60, 10.59 ± 0.91, 11.86 ± 1.96, and 11.85 ± 1.28 mm^2 have been obtained for the rGO, Au@rGO, Ag@rGO, and Pt@rGO, respectively.

As expected, the CV profiles of $Ru(NH_3)_6^{3+/2+}$ (Figure S7B) evidenced a slight signal improvement for MNPs@rGO compared with the rGO, while a significant ΔE reduction was observed (see Table S2). No relevant differences among MNPs were recorded since the ruthenium acts as an outer-sphere redox probe, and for this reason, the different MNPs give similar responses.[68]

Finally, the resistance to the electron transfer was also studied with EIS; the Nyquist plot (Figure 5F) evidences a substantial difference between the rGO- and the MNPs@rGO-based sensors. Indeed, the rGO gives rise to the typical semicircle with an R_{ct} of 1.9 KΩ (calculated with the Randles equivalent circuit), while the MNPs@rGO appears in the Nyquist plot as straight lines, clearly indicating the reduction of the electron transfer resistance.[65,71,72]

MNPs@rGO Sensor Application. After proving the MNPs@rGO superior performance compared to conventional electrochemical probes, the sensors were used to detect various analytes of food, biological, and environmental interest to assess their potentiality in real analysis. In particular, caffeic acid (CA), nitrite (NO_2^-), and hydrogen peroxide (H_2O_2) were analyzed in model solution and real samples/applications; for each analyte, the most suitable sensor was used. Before working with the analytes, the exploitable working potential window for each sensor was explored in the related measuring buffer. The rGO-, Au@rGO-, and Pt@rGO-based sensors were able to work in the −0.5 V/+1.0 V range, while the Ag@rGO was usable between +0.3 and + 1.0 V because of the presence of the typical Ag redox peaks. In Figure 6A−C, the CVs that run in the presence of the target analyte are shown, where the Au@rGO-, Ag@rGO-, and Pt@rGO-based sensors were employed to measure the CA (Figure 6A), NO_2^- (Figure 6B), and H_2O_2 (Figure 6C), respectively; bare rGO was used as the control.

CA cyclic voltammograms performed with the Au@rGO sensor show a defined reversible behavior, and the obtained peaks appear significantly improved compared with the bare rGO (Figure 6A). The same trend was observed for the NO_2^-, analyzed with the Ag@rGO sensor, where a greater oxidation current than in bare rGO was observed (Figure 6B). The anodic peak shift to lower overpotential ($\Delta E \sim 26$ mV) suggests that the Ag enhances the electron transfer kinetics for the NO_2^- oxidation.[73] On the other hand, the Pt@rGO allows direct analysis of H_2O_2 (Figure 6C); in this case, a large irreversible cathodic peak at low negative potentials is obtained: this electrochemistry is typical of the H_2O_2 reduction catalyzed by Pt nanostructures.[74] In this case, the bare rGO does not provide any response, since it is unable to assist the H_2O_2 reduction.

CA and NO_2^- were also analyzed using DPV (Figure 6D,E). In both cases, for increasing amounts of analyte, proportional, reproducible (RSD ≤ 12.5%, n = 3), and defined anodic peak

https://doi.org/10.1021/acssensors.2c01782
ACS Sens. 2023, 8, 598−609

currents were observed at an overpotential of 0.18 and 0.77 V, respectively.

As shown in Figure 6D insets and in Figure S8, excellent linearity for the CA and NO_2^- was obtained in the range of 0.5−100 μM ($y/\mu A = 0.0351x/\mu M + 0.0298/\mu A$; $R^2 = 0.999$) and 1−100 μM ($y/\mu A = 0.0197x/\mu M + 0.0117/\mu A$; $R^2 = 0.999$), respectively.

The inclusion of Au- and AgNPs significantly improves the electroanalytical performances of the rGO, enabling superior sensitivity (see the slopes of the calibration curves in Figure S8). An LOD of 50 and 120 nM was obtained for the CA and NO_2^-, respectively; the LOD was calculated according to the following formula: LOD = $[(3\sigma)/m]$, where σ is the standard deviation of the y-intercept and "m" is the slope of the linear regression.

As proof of applicability, the Au@rGO and Ag@rGO sensors were used for CA-like compound identification in the coffee extract and NO_2^- quantification in fishing lake water. CA is a phenolic compound with a hydroxycinnamic structure characterized by an extreme antioxidant capacity, due to its ortho-phenolic moiety. Coffee is a food rich in polyphenols—in particular, CA and CA-like molecules[75,76]—for this reason, the quantification of these molecules can indicate the antioxidant capacity of coffee. Before the CA quantification via the Au@rGO sensor, the phenolic profile of the coffee sample was characterized by liquid chromatography-tandem mass spectrometry; o-diphenols, with a cinnamic structure, were found to be the most abundant phenols (∼134.3 mg caffeic acid equiv L^{-1}). The coffee sample was treated before measurement, as reported in Section S1.2, and the extract was properly diluted and measured with the Au@rGO sensor. To test the ability of the sensor to properly quantify CA, the sample was fortified at three CA levels. The data obtained are reported in Table S3: in all the cases, the overpotential registered is close to 0.18 V (±0.01 V), confirming the presence of endogenous CA-like compounds; good recoveries were obtained for all the fortifications (103−110%).

In contrast, NO_2^- is an inorganic pollutant, toxic to human health, and widely used in agriculture as a fertilizer.[77] The World Health Organization (WHO) establishes 0.5 ppm (∼10.9 μM) as the maximum residual limit (MRL) in drinking water;[73] from this arises the need to monitor this compound in the environmental waters. Thus, we applied the Ag@rGO sensor to the NO_2^- quantification in lake water samples. The water was spiked at three NO_2^- concentration levels consistent with the MRL (i.e., lower, equal, and higher); the unfortified sample did not give any signal, excluding the presence of interferers. In all cases, good recoveries were obtained (101−113%) (Table S3), and the recorded overpotential was close to 0.77 V (±0.02 V) in all measurements.

For both CA and NO_2^- analyses, the sensors provided extremely reproducible results ($RSD_{Au@rGO}$ = 6.3% and $RSD_{Ag@rGO}$ = 8.1%, n = 20), resulting in a reusable and not affected by fouling sensor surface.

Resistance to passivation of the sensors was evaluated by 20 consecutive measurements of coffee and lake water samples spiked with 7.5 μM CA and 40 μM NO_2^-, respectively. The measurements were performed without washing the electrode surface for consecutive DPVs. For both CA and NO_2^- determination, the sensors provided extremely reproducible results ($RSD_{Au@rGO}$ = 6.3% and $RSD_{Ag@rGO}$ = 8.1%, n = 20), resulting to be reusable and not affected by fouling.

Concerning the Pt@rGO sensor, to improve its sensitivity for H_2O_2 detection, chronoamperometry was employed. Initially, the working potential was studied by exploring the range from 0.2 down to −0.4 V; 0.0 V was selected as a compromise between signal intensity and reproducibility. To maximize the electrocatalytic performances, a pretreatment of the electrode at +0.8 V (60 s) was applied before the measurement. This strategy allows PtNPs to exert a higher catalytic activity since the presence of platinum oxides is disfavored and the oxide-free Pt surface is more prone to assist the H_2O_2 reduction to H_2O.[74] The cathodic current, which was employed as the analytical signal, can be ascribed to the Pt surface regeneration after H_2O_2 adsorption and conversion to H_2O.

Figure 6F reports the chronoamperometric curves recorded during the calibration; the Pt@rGO sensor gave reproducible (RSD ≤ 10.5%, n = 3) cathodic currents proportional to the amount of H_2O_2 analyzed. On the other hand, no significant cathodic currents were observed for the bare rGO, definitely proving the nanozyme role of the Pt nanostructures. The sensor allows the determination of H_2O_2 between 5 and 2000 μM ($y/\mu A = 0.0045x/\mu M - 0.1274/\mu A$; $R^2 = 0.997$), showing an LOD of 0.6 μM; the calibration curve is shown in Figure S8.

Then, the Pt@rGO sensors were used to detect H_2O_2 surface residues after environmental fogging; the treatment was conducted following the EU and WHO recommendations on COVID-19 prevention,[32,78] and a detailed description of the treatment can be found in Section S1.2. In brief, the H_2O_2 residues' decay onto a laboratory desk surface was evaluated immediately after the fogging and after 15 and 30 min. Table S3 reports the results obtained, and the decay of the H_2O_2 residue was observed to be consistent with the treatment time. To demonstrate the sensor accuracy, the analyzed surface was also spiked with three levels of H_2O_2 for each treatment time; the very good recovery rate recorded (90−112%) proves the sensor's suitability for this application. Eventually, the Pt@rGO-based sensor reusability was tested by measuring 10 consecutive times surfaces subjected to fogging treatment spiked with 60 μM H_2O_2; the data prove the reusability of the sensor, which did not suffer passivation (RSD = 7.1%, n = 10).

Focusing on the literature of sensors based on laser-induced graphene (LIG) and rGO, both pristine and decorated with MNPs, the performance of the developed sensors is better or comparable (Table S4). For the three developed sensors and the relative applications, the LODs are lower than the majority of the studies reported in the literature, demonstrating that the proposed strategy returns effective sensing surfaces able, at the same time, to act also as transducers. The latter is a relevant issue since rGO is commonly deposited on transducers/electrodes, while in the case of the LIG, the modified surface is often used directly as the sensing layer. In this work, we have produced transferable films that can be designed with the desired shape and potentially transferred on different substrates. For the sake of clarity, we want to underline that the performance of the Au@rGO was compared with sensors that have been employed for the determination of ortho-phenolic compounds; no paper in the literature reports the determination of CA with LIG or rGO-based sensors. Overall, the obtained performance can be ascribed to the presence of naked noble MNPs uniformly distributed on a highly exfoliated rGO film; the rGO film ensures an excellent electron transfer ability, while the MNPs give additional electrocatalytic activities. As shown in Table S4, the rGO and LIG decoration is often obtained using additional and dedicated strategies (i.e., sputtering, electrodeposition, etc.); in this case, the decoration strategy does not need external MNP synthesis, and the MNPs do not require capping agents, are

https://doi.org/10.1021/acssensors.2c01782
ACS Sens. 2023, 8, 598−609

reproducible, and occur in few seconds concurrently to the rGO formation, giving rise to transferable freestanding films.

CONCLUSIONS

Herein, a straightforward technique to produce freestanding films of rGO embedding naked-MNPs is proposed. The produced MNPs@rGO films are easily transferable onto flexible plastic supports to obtain transducers and functional sensing surfaces, which result in enhanced stand-alone lab-made sensors. The nanocomposite-based films are obtained using a CO_2 laser plotter, which allows the controlled formation of hierarchic 2D/0D structures with high resolution. This approach enables the formation of naked Au, Ag, and Pt regularly shaped nanostructures, uniformly distributed along with a highly exfoliated rGO film. As opposed to commonly used methods, our technique does not require multistep and cumbersome procedures to form and decorate rGO-nanostructures and capping agents and/or external synthesis is not needed to generate MNPs, and the laser treatments drive the uniform distribution of MNPs on the whole rGO film.

We demonstrated the potentiality of MNPs@rGO-based sensors for detecting different analytes in various samples and thus for real-world applications. The sensors benefit from the MNP features, which are enhanced by the highly exfoliated rGO hosting substrate, also allowing us to obtain extra catalytic activity concerning the bare-rGO, as proved in the case of the Pt-containing rGO nanocomposite.

All in all, the proposed strategy is freestanding from the hosting support, leading to the nanofilms' ubiquitous transfer onto different substrates. The produced MNPs are naked and therefore are potentially modifiable with different molecules. MNPs@rGO films will be further explored in a near future since they could offer outstanding solutions and new opportunities in the (bio)sensoristic scenario and active substrates in different optoelectronic devices (i.e., supercapacitor, field-effect transistor, SERS substrates, etc.) and applications (i.e., diagnostic, bioimaging, etc.).

ASSOCIATED CONTENT

Supporting Information

The Supporting Information is available free of charge at https://pubs.acs.org/doi/10.1021/acssensors.2c01782.

Reagents and stock solutions; sample processing and fogging treatment; laser treatment optimization on the graphene oxide film; optimization of the MNPs@rGO film fabrication. SEM of the GO film before and after the laser scribing process; SEM micrograph of the GO film before the laser scribing process; elemental mapping and EDX analysis of Au@rGO, Ag@rGO, and Pt@rGO; XPS spectra of the M^{n+}@GO films before the laser scribing process; cyclic voltammogram of the rGO sensor in 0.1 M KCl; SEM micrographs and peak intensity obtained via CV to assess sensor stability and storability; cyclic voltammograms of 3 mM $Fe(CN)_6^{4-/3-}$ in 0.1 M KCl and 3 mM $Ru(NH_3)_6^{3+/2+}$ in 0.1 M KCl performed with the rGO, Au@rGO; Ag@rGO, and Pt@rGO sensors; calibration curves of caffeic acid, sodium nitrite, and hydrogen peroxide performed with Au@rGO, Ag@rGO, and Pt@rGO sensors; sensor components' size; optimization of the laser parameters and nanoarchitecture precursors; electrochemical features of the rGO and MNPs@rGO-based sensors; caffeic acid, sodium nitrite, and hydrogen peroxide determination in samples; and sensor performance comparison tables with respect to the literature (PDF)

rGO-based conductive film patterning, fabrication, and transferring (AVI)

AUTHOR INFORMATION

Corresponding Authors

Ruslan Álvarez-Diduk − *Nanobioelectronics & Biosensors Group, Catalan Institute of Nanoscience and Nanotechnology (ICN2) CSIC and BIST, Bellaterra 08193 Barcelona, Spain;* orcid.org/0000-0002-9876-1574; Email: ruslan.alvarez@icn2.cat

Arben Merkoçi − *Nanobioelectronics & Biosensors Group, Catalan Institute of Nanoscience and Nanotechnology (ICN2) CSIC and BIST, Bellaterra 08193 Barcelona, Spain; ICREA Institució Catalana de Recerca i Estudis Avançats, Passeig Lluís Companys 23, 08010 Barcelona, Spain;* orcid.org/0000-0003-2486-8085; Email: arben.merkoci@icn2.cat

Authors

Annalisa Scroccarello − *Nanobioelectronics & Biosensors Group, Catalan Institute of Nanoscience and Nanotechnology (ICN2) CSIC and BIST, Bellaterra 08193 Barcelona, Spain; Department of Bioscience and Technology for Food, Agriculture and Environment, University of Teramo, 64100 Teramo, Italy*

Flavio Della Pelle − *Department of Bioscience and Technology for Food, Agriculture and Environment, University of Teramo, 64100 Teramo, Italy;* orcid.org/0000-0002-8877-7580

Cecilia de Carvalho Castro e Silva − *Nanobioelectronics & Biosensors Group, Catalan Institute of Nanoscience and Nanotechnology (ICN2) CSIC and BIST, Bellaterra 08193 Barcelona, Spain; MackGraphe—Mackenzie Institute for Research in Graphene and Nanotechnologies, Mackenzie Presbyterian University, 01302-907 São Paulo, Brazil;* orcid.org/0000-0003-3933-1838

Andrea Idili − *Nanobioelectronics & Biosensors Group, Catalan Institute of Nanoscience and Nanotechnology (ICN2) CSIC and BIST, Bellaterra 08193 Barcelona, Spain; Department of Chemical Science and Technologies, Tor Vergata University of Rome, 00133 Roma, Italy*

Claudio Parolo − *Nanobioelectronics & Biosensors Group, Catalan Institute of Nanoscience and Nanotechnology (ICN2) CSIC and BIST, Bellaterra 08193 Barcelona, Spain*

Dario Compagnone − *Department of Bioscience and Technology for Food, Agriculture and Environment, University of Teramo, 64100 Teramo, Italy;* orcid.org/0000-0001-7849-8943

Complete contact information is available at: https://pubs.acs.org/10.1021/acssensors.2c01782

Author Contributions

#A.S. and R.A.-D. contributed equally to this work. All authors have given approval to the final version of the manuscript.

Notes

The authors declare no competing financial interest.

ACKNOWLEDGMENTS

R.A.-D. acknowledges funding from the European Union Horizon 2020 Programme under grant no. 881603 (Graphene Flagship Core 3). ICN2 is funded by CERCA Programme,

Generalitat de Catalunya. Grant SEV-2017-0706 is funded by MCIN/AEI/10.13039/501100011033. The authors also acknowledge the project PID2021-124795NB-I00 funded by MCIN/AEI/10.13039/501100011033/and FEDER Una manera de hacer Europa. F.D.P. and D.C. acknowledge the Ministry of Education, University and Research (MIUR) and European Social Fund (ESF) for the PON R&I 2014e2020 program, action 1.2 0AIM: Attraction and International Mobility' (AIM1894039-3). C.C.C.S. acknowledges funding through CAPES—PRINT (Programa Institucional de Internacionalização; grant #88887.310281/2018-00 and 88887.467442/2019-00) and Mackpesquisa-UPM.

REFERENCES

(1) Nasrollahzadeh, M.; Sajadi, S. M.; Sajjadi, M.; Issaabadi, Z. *An Introduction to Nanotechnology*, 1st ed.; Elsevier Ltd., 2019; Vol. *28*.
(2) Quesada-González, D.; Merkoçi, A. Nanomaterial-Based Devices for Point-of-Care Diagnostic Applications. *Chem. Soc. Rev.* **2018**, *47*, 4697−4709.
(3) Jamkhande, P. G.; Ghule, N. W.; Bamer, A. H.; Kalaskar, M. G. Metal Nanoparticles Synthesis: An Overview on Methods of Preparation, Advantages and Disadvantages, and Applications. *J. Drug Deliv. Sci. Technol.* **2019**, *53*, 101174.
(4) Patil, P. O.; Pandey, G. R.; Patil, A. G.; Borse, V. B.; Deshmukh, P. K.; Patil, D. R.; Tade, R. S.; Nangare, S. N.; Khan, Z. G.; Patil, A. M.; More, M. P.; Veerapandian, M.; Bari, S. B. Graphene-Based Nanocomposites for Sensitivity Enhancement of Surface Plasmon Resonance Sensor for Biological and Chemical Sensing: A Review. *Biosens. Bioelectron.* **2019**, *139*, 111324.
(5) Huang, N.; Xu, E.; Xie, J.; Liu, Y.; Deng, Z.; Wang, J.; Liu, Z.; Tian, J.; Liu, Y.; Ye, Q. A Sliver Deposition Signal-Enhanced Optical Biomolecular Detection Device Based on Reduced Graphene Oxide. *Talanta* **2022**, *249*, 123691.
(6) Della Pelle, F.; Rojas, D.; Silveri, F.; Ferraro, G.; Fratini, E.; Scroccarello, A.; Escarpa, A.; Compagnone, D. Class-Selective Voltammetric Determination of Hydroxycinnamic Acids Structural Analogs Using a WS2/Catechin-Capped AuNPs/Carbon Black−Based Nanocomposite Sensor. *Microchim. Acta* **2020**, *187*, 296.
(7) Nagar, B.; Balsells, M.; de la Escosura-Muñiz, A.; Gomez-Romero, P.; Merkoçi, A. Fully Printed One-Step Biosensing Device Using Graphene/AuNPs Composite. *Biosens. Bioelectron.* **2019**, *129*, 238−244.
(8) Nazarpour, S.; Hajian, R.; Sabzvari, M. H. A Novel Nanocomposite Electrochemical Sensor Based on Green Synthesis of Reduced Graphene Oxide/Gold Nanoparticles Modified Screen Printed Electrode for Determination of Tryptophan Using Response Surface Methodology Approach. *Microchem. J.* **2020**, *154*, 104634.
(9) Zhang, D.; Yang, Z.; Li, P.; Pang, M.; Xue, Q. Flexible Self-Powered High-Performance Ammonia Sensor Based on Au-Decorated MoSe2 Nanoflowers Driven by Single Layer MoS2-Flake Piezoelectric Nanogenerator. *Nano Energy* **2019**, *65*, 103974.
(10) Zhang, D.; Wang, D.; Li, P.; Zhou, X.; Zong, X.; Dong, G. Facile Fabrication of High-Performance QCM Humidity Sensor Based on Layer-by-Layer Self-Assembled Polyaniline/Graphene Oxide Nanocomposite Film. *Sens. Actuators, B* **2018**, *255*, 1869−1877.
(11) Zhang, D.; Liu, J.; Jiang, C.; Liu, A.; Xia, B. Quantitative Detection of Formaldehyde and Ammonia Gas via Metal Oxide-Modified Graphene-Based Sensor Array Combining with Neural Network Model. *Sens. Actuators, B* **2017**, *240*, 55−65.
(12) Wang, D.; Zhang, D.; Mi, Q. A High-Performance Room Temperature Benzene Gas Sensor Based on CoTiO3 Covered TiO2 Nanospheres Decorated with Pd Nanoparticles. *Sens. Actuators, B* **2022**, *350*, 130830.
(13) Silveri, F.; Della Pelle, F.; Scroccarello, A.; Ain Bukhari, Q. U.; Del Carlo, M.; Compagnone, D. Modular Graphene Mediator Film-Based Electrochemical Pocket Device for Chlorpyrifos Determination. *Talanta* **2022**, *240*, 123212.
(14) Coroş, M.; Pogăcean, F.; Măgeruşan, L.; Socaci, C.; Pruneanu, S. A Brief Overview on Synthesis and Applications of Graphene and Graphene-Based Nanomaterials. *Front. Mater. Sci.* **2019**, *13*, 23−32.
(15) Chua, C. K.; Pumera, M. Chemical Reduction of Graphene Oxide: A Synthetic Chemistry Viewpoint. *Chem. Soc. Rev.* **2014**, *43*, 291−312.
(16) Zhang, Z.; Fraser, A.; Ye, S.; Merle, G.; Barralet, J. Top-down Bottom-up Graphene Synthesis. *Nano Futures* **2019**, *3*, 042003.
(17) Zhu, Q. L.; Xu, Q. Immobilization of Ultrafine Metal Nanoparticles to High-Surface-Area Materials and Their Catalytic Applications. *Chem* **2016**, *1*, 220−245.
(18) Barsan, M. M.; Brett, C. M. A. Recent Advances in Layer-by-Layer Strategies for Biosensors Incorporating Metal Nanoparticles. *Trac. Trends Anal. Chem.* **2016**, *79*, 286−296.
(19) Rane, A. V.; Kanny, K.; Abitha, V. K.; Thomas, S. Methods for Synthesis of Nanoparticles and Fabrication of Nanocomposites. *Synthesis of Inorganic Nanomaterials*; Woodhead Publishing, 2018; pp 121−139.
(20) Tran, M.; Roy, S.; Kmiec, S.; Whale, A.; Martin, S.; Sundararajan, S.; Padalkar, S. Formation of Size and Density Controlled Nanostructures by Galvanic Displacement. *Nanomaterials* **2020**, *10*, 644.
(21) Ramesh, G. V.; Porel, S.; Radhakrishnan, T. P. Polymer Thin Films Embedded with in Situ Grown Metal Nanoparticles. *Chem. Soc. Rev.* **2009**, *38*, 2646−2656.
(22) Zhu, L.; Gao, Y. Y.; Han, B.; Liu, S.; Fu, X. Y.; Ding, H.; Zhang, Y. L. Programmable Laser Patterning of Ag Nanoparticles and Reduced Graphene Oxide Hybrid Electrodes for Nonenzymatic Hydrogen Peroxide Detection. *ACS Appl. Nano Mater.* **2019**, *2*, 7989−7996.
(23) You, Z.; Qiu, Q.; Chen, H.; Feng, Y.; Wang, X.; Wang, Y.; Ying, Y. Laser-Induced Noble Metal Nanoparticle-Graphene Composites Enabled Flexible Biosensor for Pathogen Detection. *Biosens. Bioelectron.* **2020**, *150*, 111896.
(24) Li, G. Direct Laser Writing of Graphene Electrodes. *J. Appl. Phys.* **2020**, *127*, 010901.
(25) Griffiths, K.; Dale, C.; Hedley, J.; Kowal, M. D.; Kaner, R. B.; Keegan, N. Laser-Scribed Graphene Presents an Opportunity to Print a New Generation of Disposable Electrochemical Sensors. *Nanoscale* **2014**, *6*, 13613−13622.
(26) You, R.; Liu, Y. Q.; Hao, Y. L.; Han, D. D.; Zhang, Y. L.; You, Z. Laser Fabrication of Graphene-Based Flexible Electronics. *Adv. Mater.* **2020**, *32*, 1901981.
(27) Giacomelli, C.; Álvarez-Diduk, R.; Testolin, A.; Merkoçi, A. Selective Stamping of Laser Scribed RGO Nanofilms: From Sensing to Multiple Applications. *2D Mater.* **2020**, *7*, 024006.
(28) Kurra, N.; Jiang, Q.; Nayak, P.; Alshareef, H. N. Laser-Derived Graphene: A Three-Dimensional Printed Graphene Electrode and Its Emerging Applications. *Nano Today* **2019**, *24*, 81−102.
(29) Lin, J.; Peng, Z.; Liu, Y.; Ruiz-Zepeda, F.; Ye, R.; Samuel, E. L. G.; Yacaman, M. J.; Yakobson, B. I.; Tour, J. M. Laser-Induced Porous Graphene Films from Commercial Polymers. *Nat. Commun.* **2014**, *5*, 5714.
(30) Ye, R.; Peng, Z.; Wang, T.; Xu, Y.; Zhang, J.; Li, Y.; Nilewski, L. G.; Lin, J.; Tour, J. M. In Situ Formation of Metal Oxide Nanocrystals Embedded in Laser-Induced Graphene. *ACS Nano* **2015**, *9*, 9244−9251.
(31) Sen, B.; Kuzu, S.; Demir, E.; Akocak, S.; Sen, F. Polymer-graphene hybride decorated Pt nanoparticles as highly efficient and reusable catalyst for the dehydrogenation of dimethylamine-borane at room temperature. *Int. J. Hydrogen Energy* **2017**, *42*, 23284−23291.
(32) Scroccarello, A.; Della Pelle, F.; Del Carlo, M.; Compagnone, D. Monitoring Disinfection in the Covid-19 Era. A Reagent-Free Nanostructured Smartphone-Based Device for the Detection of Oxidative Disinfectants. *Microchem. J.* **2022**, *175*, 107165.
(33) Dresselhaus, M. S.; Jorio, A.; Hofmann, M.; Dresselhaus, G.; Saito, R. Perspectives on Carbon Nanotubes and Graphene Raman Spectroscopy. *Nano Lett.* **2010**, *10*, 751−758.

https://doi.org/10.1021/acssensors.2c01782
ACS Sens. 2023, 8, 598−609

(34) Liu, J.; Ma, Q.; Huang, Z.; Liu, G.; Zhang, H. Recent Progress in Graphene-Based Noble-Metal Nanocomposites for Electrocatalytic Applications. *Adv. Mater.* **2019**, *31*, 1800696.
(35) Moussa, S.; Abdelsayed, V.; Samy El-Shall, M. Laser Synthesis of Pt, Pd, CoO and Pd-CoO Nanoparticle Catalysts Supported on Graphene. *Chem. Phys. Lett.* **2011**, *510*, 179−184.
(36) Hao, Y.; Wang, Y.; Wang, L.; Ni, Z.; Wang, Z.; Wang, R.; Koo, C. K.; Shen, Z.; Thong, J. T. L. Probing Layer Number and Stacking Order of Few-Layer Graphene by Raman Spectroscopy. *Small* **2010**, *6*, 195−200.
(37) Fornasini, L.; Scaravonati, S.; Magnani, G.; Morenghi, A.; Sidoli, M.; Bersani, D.; Bertoni, G.; Aversa, L.; Verucchi, R.; Riccò, M.; Lottici, P. P.; Pontiroli, D. In Situ Decoration of Laser-Scribed Graphene with TiO2 Nanoparticles for Scalable High-Performance Micro-Supercapacitors. *Carbon* **2021**, *176*, 296−306.
(38) Mazzotta, E.; Rella, S.; Turco, A.; Malitesta, C. XPS in Development of Chemical Sensors. *RSC Adv.* **2015**, *5*, 83164−83186.
(39) Rodrigues, J.; Zanoni, J.; Gaspar, G.; Fernandes, A. J. S.; Carvalho, A. F.; Santos, N. F.; Monteiro, T.; Costa, F. M. ZnO Decorated Laser-Induced Graphene Produced by Direct Laser Scribing. *Nanoscale Adv.* **2019**, *1*, 3252−3268.
(40) Yang, M. Q.; Pan, X.; Zhang, N.; Xu, Y. J. A Facile One-Step Way to Anchor Noble Metal (Au, Ag, Pd) Nanoparticles on a Reduced Graphene Oxide Mat with Catalytic Activity for Selective Reduction of Nitroaromatic Compounds. *CrystEngComm* **2013**, *15*, 6819−6828.
(41) Zhao, G.; Zhu, H. Cation−π Interactions in Graphene-Containing Systems for Water Treatment and Beyond. *Adv. Mater.* **2020**, *32*, 1905756.
(42) Wang, J.; Dong, X.; Xu, R.; Li, S.; Chen, P.; Chan-Park, M. B. Template-Free Synthesis of Large Anisotropic Gold Nanostructures on Reduced Graphene Oxide. *Nanoscale* **2012**, *4*, 3055−3059.
(43) Zan, R.; Bangert, U.; Ramasse, Q.; Novoselov, K. S. Evolution of Gold Nanostructures on Graphene. *Small* **2011**, *7*, 2868−2872.
(44) Pramanik, G.; Humpolickova, J.; Valenta, J.; Kundu, P.; Bals, S.; Bour, P.; Dracinsky, M.; Cigler, P. Gold Nanoclusters with Bright Near-Infrared Photoluminescence. *Nanoscale* **2018**, *10*, 3792−3798.
(45) Kar, P.; Chang, T. S.; Chen, C. Y.; Chen, J. S.; Yi, S.; Sutradhar, S.; Liao, W. S. Fluorescence Turn-On Antioxidant Recognition by Interface-Mediated Radical Termination of l -Cysteine-Capped Gold Nanoclusters. *ACS Appl. Nano Mater.* **2021**, *4*, 3360−3368.
(46) Han, H.; Pan, D.; Wang, C.; Zhu, R. Controlled Synthesis of Dendritic Gold Nanostructures by Graphene Oxide and Their Morphology-Dependent Performance for Iron Detection in Coastal Waters. *RSC Adv.* **2017**, *7*, 15833−15841.
(47) Kim, Y. K.; Na, H. K.; Lee, Y. W.; Jang, H.; Han, S. W.; Min, D. H. The Direct Growth of Gold Rods on Graphene Thin Films. *Chem. Commun.* **2010**, *46*, 3185−3187.
(48) Marangoni, V. S.; Germano, L. D.; Silva, C. C. C.; de Souza, E. A.; Maroneze, C. M. Engineering Two-Dimensional Gold Nanostructures Using Graphene Oxide Nanosheets as a Template. *Nanoscale* **2018**, *10*, 13315−13319.
(49) Carlini, L.; Fasolato, C.; Postorino, P.; Fratoddi, I.; Venditti, I.; Testa, G.; Battocchio, C. Comparison between Silver and Gold Nanoparticles Stabilized with Negatively Charged Hydrophilic Thiols: SR-XPS and SERS as Probes for Structural Differences and Similarities. *Colloids Surf., A* **2017**, *532*, 183−188.
(50) Sahoo, S. R.; Ke, S. C. Spin-Orbit Coupling Effects in Au 4f Core-Level Electronic Structures in Supported Low-Dimensional Gold Nanoparticles. *Nanomaterials* **2021**, *11*, 554.
(51) Zhou, B.; Zhao, X.; Liu, H.; Qu, J.; Huang, C. P. Synthesis of Visible-Light Sensitive M-BiVO4 (M = Ag, Co, and Ni) for the Photocatalytic Degradation of Organic Pollutants. *Sep. Purif. Technol.* **2011**, *77*, 275−282.
(52) Mao, Y.; Yang, Y.; Meng, X.; Hu, C.; Wang, C.; Wei, J.; Yang, H. A Facile Approach to Prepare Novel Coral-like Ag3C6H5O7 Microstructures for Surface-Enhanced Raman Scattering. *Chem. Lett.* **2016**, *45*, 232−234.
(53) Casaletto, M. P.; Longo, A.; Martorana, A.; Prestianni, A.; Venezia, A. M. XPS Study of Supported Gold Catalysts: The Role of Au0 and Au+d Species as Active Sites. *Surf. Interface Anal.* **2006**, *38*, 215−218.
(54) Fontana, L.; Bassetti, M.; Battocchio, C.; Venditti, I.; Fratoddi, I. Synthesis of Gold and Silver Nanoparticles Functionalized with Organic Dithiols. *Colloids Surf., A* **2017**, *532*, 282−289.
(55) Tian, Z. Q.; Jiang, S. P.; Liang, Y. M.; Shen, P. K. Synthesis and Characterization of Platinum Catalysts on Multiwalled Carbon Nanotubes by Intermittent Microwave Irradiation for Fuel Cell Applications. *J. Phys. Chem. B* **2006**, *110*, 5343−5350.
(56) Romanchenko, A.; Likhatski, M.; Mikhlin, Y. X-Ray Photoelectron Spectroscopy (XPS) Study of the Products Formed on Sulfide Minerals upon the Interaction with Aqueous Platinum (IV) Chloride Complexes. *Minerals* **2018**, *8*, 578.
(57) Proa-Coronado, S.; Vargas-García, J. R.; Manzo-Robledo, A.; Mendoza-Acevedo, S.; Villagómez, C. J.; Mercado-Zúñiga, C.; Muñoz-Aguirre, N.; Villa-Vargas, L. A.; Martinez-Rivas, A. Platinum Nanoparticles Homogenously Decorating Multilayered Reduced Graphene Oxide for Electrical Nanobiosensor Applications. *Thin Solid Films* **2018**, *658*, 54−60.
(58) Smirnov, M. Y.; Kalinkin, A. V.; Vovk, E. I.; Bukhtiyarov, V. I. Analysis of the Oxidation State of Platinum Particles in Supported Catalysts by Double Differentiation of XPS Lines. *J. Struct. Chem.* **2016**, *57*, 1127−1133.
(59) Şen, F.; Gökağaç, G. Different Sized Platinum Nanoparticles Supported on Carbon: An XPS Study on These Methanol Oxidation Catalysts. *J. Phys. Chem. C* **2007**, *111*, 5715−5720.
(60) Ghildiyal, P.; Yang, Y.; Kline, D. J.; Holdren, S.; Zachariah, M. R. Ultrafast, Scalable Laser Photothermal Synthesis and Writing of Uniformly Dispersed Metal Nanoclusters in Polymer Films. *Nanoscale* **2019**, *11*, 13354−13365.
(61) Moussa, S.; Atkinson, G.; SamyEl-Shall, M.; Shehata, A.; AbouZeid, K. M.; Mohamed, M. B. Laser Assisted Photocatalytic Reduction of Metal Ions by Graphene Oxide. *J. Mater. Chem.* **2011**, *21*, 9608−9619.
(62) Zedan, A. F.; Moussa, S.; Terner, J.; Atkinson, G.; El-Shall, M. S. Ultrasmall Gold Nanoparticles Anchored to Graphene and Enhanced Photothermal Effects by Laser Irradiation of Gold Nanostructures in Graphene Oxide Solutions. *ACS Nano* **2013**, *7*, 627−636.
(63) Yang, L.; Wei, J.; Ma, Z.; Song, P.; Ma, J.; Zhao, Y.; Huang, Z.; Zhang, M.; Yang, F.; Wang, X. The Fabrication of Micro/Nano Structures by Laser Machining. *Nanomaterials* **2019**, *9*, 1789.
(64) Han, B.; Zhang, Y. L.; Zhu, L.; Chen, X. H.; Ma, Z. C.; Zhang, X. L.; Wang, J. N.; Wang, W.; Liu, Y. Q.; Chen, Q. D.; Sun, H. B. Direct Laser Scribing of AgNPs@RGO Biochip as a Reusable SERS Sensor for DNA Detection. *Sens. Actuators, B* **2018**, *270*, 500−507.
(65) Aparicio-Martínez, E.; Ibarra, A.; Estrada-Moreno, I. A.; Osuna, V.; Dominguez, R. B. Flexible Electrochemical Sensor Based on Laser Scribed Graphene/Ag Nanoparticles for Non-Enzymatic Hydrogen Peroxide Detection. *Sens. Actuators, B* **2019**, *301*, 127101.
(66) Zhou, X.; Huang, X.; Qi, X.; Wu, S.; Xue, C.; Boey, F. Y. C.; Yan, Q.; Chen, P.; Zhang, H. In Situ Synthesis of Metal Nanoparticles on Single-Layer Graphene Oxide and Reduced Graphene Oxide Surfaces. *J. Phys. Chem. C* **2009**, *113*, 10842−10846.
(67) Perevezentseva, D. O.; Vaitulevich, E. A.; Bimatov, V. V. Synthesis of Silver Nanoparticles in the Presence of Polyethylene Glycol and Their Electrochemical Behavior at a Graphite Electrode by Cyclic Voltammetry. *Orient. J. Chem.* **2018**, *34*, 1130−1135.
(68) Tanimoto, S.; Ichimura, A. Discrimination of Inner- and Outer-Sphere Electrode Reactions by Cyclic Voltammetry Experiments. *J. Chem. Educ.* **2013**, *90*, 778−781.
(69) Silveri, F.; Pelle, F. D.; Scroccarello, A.; Mazzotta, E.; Giulio, T. D.; Malitesta, C.; Compagnone, D. Carbon Black Functionalized with Naturally Occurring Compounds in Water Phase for Electrochemical Sensing of Antioxidant Compounds. *Antioxidants* **2022**, *11*, 2008.
(70) Randviir, E. P. A cross examination of electron transfer rate constants for carbon screen-printed electrodes using Electrochemical Impedance Spectroscopy and cyclic voltammetry. *Electrochim. Acta* **2018**, *286*, 179−186.

https://doi.org/10.1021/acssensors.2c01782
ACS Sens. 2023, 8, 598−609

(71) Zhao, G.; Liu, G. Electrochemical Deposition of Gold Nanoparticles on Reduced Graphene Oxide by Fast Scan Cyclic Voltammetry for the Sensitive Determination of As(III). *Nanomaterials* **2019**, *9*, 41.
(72) Aparicio-Martínez, E.; Ibarra, A.; Estrada-Moreno, I. A.; Osuna, V.; Dominguez, R. B. Flexible Electrochemical Sensor Based on Laser Scribed Graphene/Ag Nanoparticles for Non-Enzymatic Hydrogen Peroxide Detection. *Sens. Actuators, B* **2019**, *301*, 127101.
(73) Bhat, S. A.; Pandit, S. A.; Rather, M. A.; Rather, G. M.; Rashid, N.; Ingole, P. P.; Bhat, M. A. Self-Assembled AuNPs on Sulphur-Doped Graphene: A Dual and Highly Efficient Electrochemical Sensor for Nitrite (NO2-) and Nitric Oxide (NO). *New J. Chem.* **2017**, *41*, 8347−8358.
(74) Mazzotta, E.; Di Giulio, T.; Mastronardi, V.; Pompa, P. P.; Moglianetti, M.; Malitesta, C. Bare Platinum Nanoparticles Deposited on Glassy Carbon Electrodes for Electrocatalytic Detection of Hydrogen Peroxide. *ACS Appl. Nano Mater.* **2021**, *4*, 7650−7662.
(75) Król, K.; Gantner, M.; Tatarak, A.; Hallmann, E. The Content of Polyphenols in Coffee Beans as Roasting, Origin and Storage Effect. *Eur. Food Res. Technol.* **2020**, *246*, 33−39.
(76) Madhava Naidu, M.; Sulochanamma, G.; Sampathu, S. R.; Srinivas, P. Studies on Extraction and Antioxidant Potential of Green Coffee. *Food Chem.* **2008**, *107*, 377−384.
(77) Petrova, E.; Gluhcheva, Y.; Pavlova, E.; Vladov, I.; Voyslavov, T.; Ivanova, J. Effect of Acute Sodium Nitrite Intoxication on Some Essential Biometals in Mouse Spleen. *J. Trace Elem. Med. Biol.* **2020**, *58*, 126431.
(78) World Health Organization (WHO). *Cleaning and Disinfection of Environmental Surfaces in the Context of COVID-19: Interim Guidance 15 May 2020*, 2020.

https://doi.org/10.1021/acssensors.2c01782
ACS Sens. 2023, 8, 598−609